SCIENCE FORUM (JOURNAL OF PURE AND APPLIED SCIENCES) 26, (3) (2026), 588 - 604

Science Forum (Journal of Pure and Applied Sciences)

Journal Homepage: https://atbuscienceforum.com.ng/index.php/jpas

# *In silico* and Experimental Study of Two Hydrazones: The Impact of Positional Isomerism and Metal Complexation on Antibacterial and Antioxidant Activities

**Tenimu A, Abubakar*, Gabriel K. Obiyenwa, Suleiman Muhammed, Olalekan W. Salawu**

*Department of Chemistry, Faculty of Science, Federal University Lokoja, P.M.B 1154, Kogi State.*

Abstract

The geometric disposition of pharmacophoric groups is a critical determinant of drug efficacy and target recognition. This study investigated the influence of structural isomerism on the pharmacological performance of two isomeric hydrazone-based drug candidates, differing in the position of the pyridine nitrogen atom and an ethoxy substituent located at the ortho and para positions of an adjacent benzene ring, together with their $Fe^{3+}$ and $La^{3+}$ coordination complexes. The ligands and their corresponding metal complexes were synthesized and structurally characterized using Fourier-transform infrared (FTIR) and nuclear magnetic resonance (NMR) spectroscopy. Density Functional Theory (DFT) calculations at the B3LYP/6-311G(d,p) level, molecular docking, and ADMET modelling were employed to evaluate molecular geometry, pharmacokinetic properties, and binding interactions with *Escherichia coli* DNA Gyrase (PDB: 6F86) and human Keap1 (PDB: 4L7B). Computational predictions were validated through in vitro antibacterial and antioxidant assays. Spectroscopic characterization identified L1 as the linear isoniazid isomer, exhibiting a lower carbonyl stretching frequency (1645 $cm^{-1}$) than the kinked nicotinic hydrazide analogue (L2). Molecular docking demonstrated that the linear geometry of L1 enabled deeper penetration into the narrow DNA Gyrase binding pocket, forming a stabilizing dual-lock interaction with Glu50 and Asn46, whereas the bent geometry of L2 induced steric hindrance that reduced binding affinity, highlighting the significant influence of structural isomerism. Experimental antibacterial assays corroborated these findings, with L1 exhibiting superior activity relative to L2 and the reference drug. Although the free ligands displayed moderate antioxidant activity, the $Fe^{3+}$ complex (C1) exhibited the strongest radical-scavenging capacity, significantly outperforming C2 and the uncoordinated ligands. This enhanced activity is attributed to the redox-active iron centre and paramagnetic enolic coordination, as supported by NMR analysis. Overall, the isoniazid scaffold proved pharmacologically superior to the nicotinic hydrazide analogue, while the para-oriented pyridine nitrogen and ethoxy substituent promoted a favourable molecular architecture that enhanced antibacterial efficacy. Furthermore, coordination to $Fe^{3+}$ unlocked superior antioxidant activity, identifying C1 as a promising dual-action therapeutic lead candidate.

Keywords

Isoniazid,
Nicotinic hydrazide,
Molecular Docking,
DFT calculation,
Positional Isomerism

ISSN 1119-4618 JPAS
Faculty of Science, ATBU Bauchi

Corresponding Author: Tenimu A, Abubakar, Department of Chemistry, Faculty of Science, Federal University Lokoja, P.M.B 1154, Kogi State.
Email tenimu.abubakar@fulokoja.edu.ng 

**1.0: Introduction.**

Schiff bases continue to be attractive candidates for the development of new therapeutic agents. This is mainly due to their structural and electronic features. The structural features are easily manipulable and are generally recognized to account for diverse pharmacological properties (Mushtaq et al., 2024). They possess antimicrobial, anticancer, antioxidant, antimalarial, antiviral, and anti-inflammatory activities (Nidhi et al., 2025). Several primary amines have been used in the synthesis of Schiff bases. Isoniazid, the first line change medication for the prevention and treatment of tuberculosis, and its analogue, nicotinic hydrazides, have continued to receive attention due to their inherent biological activity and potential for enhancement upon Schiff base formation. Schiff bases generated from these hydrazides upon condensation with carbonyl containing moieties have been reported to improve their therapeutic potential and, in some cases, reduce toxicity compared to the parent drug (Reema et al., 2011).

The suitable choice of carbonyl moiety (aldehyde, ketone) for such condensation is crucial to the outcome. The choice of ethoxybenzaldehydes in the current investigation is due to the expectation that the presence of the ethoxy group and the positional isomerism of the 2- and 4-ethoxy moieties can have a crucial structural impact on physicochemical properties (Fan & Yan, 2014). They are expected to increase lipophilicity and electronic distribution of the resulting Schiff bases. Such modifications can significantly improve their interactions with biological systems and consequently their antibacterial and antioxidant activities (Nidhi et al., 2025). Coordination of these Schiff bases to metal ions can give rise to complexes with further increased lipophilicity, altered redox potential, and diverse novel mechanisms of action compared to the uncomplexed organic species. Such enhanced properties are recognised as producing antibacterial agents capable of reversing drug resistance(Waziri et al., 2025) (Frei et al., 2020). Since antibiotic drug resistance remains a global health concern, the development of antibiotics with novel mechanisms of action is the identified solution, and metal complexes, because of their redox potential, are promising candidates.

Gaining deeper insights into the structure-activity relationship as well as the underlying mechanism of action of a drug candidate in a timely, efficient, and cost-effective approach requires both experimental and theoretical methods. Such comprehensive theoretical quantum chemical calculations will help elucidate the mechanism of action of the most promising compounds. To enable rapid conclusions about potential therapeutic applications, the investigation of the toxicity and pharmacokinetic properties of candidate compounds is always considered.

**2.0: Methodology**

Nicotinic hydrazide, isonicotinic hydrazide, and lanthanum (III) chloride were procured from Sigma Aldrich-Merck. Ethanol, Methanol, iron (III) chloride, and all other chemicals used are all-purpose reagents available at the Chemistry laboratory of the Federal University, Lokoja.

**Ligand Synthesis**

The preparation of the ligands and complexes follow earlier protocol

(E)-N'-(4-ethoxybenzylidene) isonicotinohydrazide hydrate (L1)

Isonicotinic hydrazide (0.255 g; 0.5 M) was dissolved in ethanol, followed by a dropwise addition of an ethanolic solution of 4-ethoxy benzaldehyde (0.279 g; 0.5 M). The colourless solution, which turned yellow, was refluxed for 6 h. On completion, the colour changed to orange. The volume of the final mixture was reduced to half and left for evaporation at room temperature. The solids were washed with solvents, recrystallized with a minimal quantity of ethanol, and dried in a vacuum desiccator. The product was weighed (0.377g (yield = 75.4%)). $^1$H NMR (400 MHz, DMSO) δ 11.92 (s, 1H), 8.79 (s, 2H), 8.41 (s, 1H), 7.82 (d, *J* = 4.8 Hz, 2H), 7.73 – 7.65 (m, 2H), 7.06 – 6.98 (m, 2H), 4.09 (p, *J* = 6.9 Hz, 2H), 1.35 (t, *J* = 7.0 Hz, 3H).

(E)-N'-(2-ethoxybenzylidene)
nicotinohydrazide hydrate (L2)

Stoichiometric amounts of ethanolic solutions of nicotinic hydrazide (0.506g; 0.5 M) and 2-ethoxy benzaldehyde (0.554g; 0.5 M) were mixed. The resulting solution was refluxed for 6 h. On completion, the colourless mixture changed to orange. The volume of the final mixture was reduced to half and left for evaporation at room temperature to form crystals. The crystals were washed with solvents, recrystallized with a minimal quantity of ethanol, and dried in a vacuum desiccator. The product was weighed. (0.391g (yield = 78.2%) $^1$H NMR (400 MHz, DMSO) δ 12.04 (s, 1H), 9.12 (s, 1H), 8.81 (s, 1H), 8.35 (s, 1H), 7.90 (dd, *J* = 7.7, 1.7 Hz, 1H), 7.64 (s, 1H), 7.47 – 7.38 (m, 1H), 7.11 (d, *J* = 8.4 Hz, 1H), 7.03 (t, *J* = 7.5 Hz, 1H), 4.15 (q, *J* = 6.9 Hz, 2H), 2.09 (s, 4H), 1.40 (t, *J* = 6.9 Hz, 3H).

**Synthesis of Complexes**

**Synthesis of FeL1n (C1)**

Iron(III) chloride solution (0.016g, 0.10 mmol) in a clean beaker was added dropwise to an ethanolic solution (25ml) of L1 (0.027g, 0.10 mmol). The resulting green solution, which changed to dark blue, was refluxed for 4 h. The precipitated complex was filtered, washed with alcohol, followed by petroleum ether, and dried in a vacuum desiccator over calcium chloride. $^1$H NMR (400 MHz, DMSO) δ 11.92 (s, 1H), 8.81 – 8.70 (m, 2H), 8.42 (s, 1H), 7.85 – 7.79 (m, 2H), 7.73 – 7.63 (m, 2H), 7.06 – 6.98 (m, 2H), 4.09 (p, *J* = 6.9 Hz, 2H), 1.35 (t, *J* = 7.0 Hz, 3H).

**Synthesis of LaL2n (C2)**

Ethanolic solution of lanthanum (III) chloride (0.025g, 0.10 mmol) was added dropwise to a solution of L2 (0.081g, 0.30 mmol). The resulting solution was refluxed for 4 h and allowed to crystallize. The precipitate was filtered, washed with alcohol, followed by petroleum ether, and dried in a vacuum desiccator over calcium chloride. $^1$H NMR (400 MHz, DMSO) δ 8.81 (s, 1H), 8.41 (s, 1H), 7.74 – 7.65 (m, 1H), 4.14 (q, *J* = 7.0 Hz, 2H), 3.50 (d, *J* = 12.3 Hz, 14H), 3.49 – 3.42 (m, 31H), 1.40 (t, *J* = 7.0 Hz, 3H).

**Antioxidant assay using DPPH**

The free radical 2,2-Diphenyl-1-Picrylhydrazyl (DPPH) was used as described (Arogba & Omede, 2012).

**Preparation of samples**

For each sample, 1 g was weighed into a flask containing 50 ml of methanol and placed on an orbital shaker and shaken for 2 h. The supernatant was carefully decanted to form the stock solution from which serial dilutions were made. 1 ml of 0.3 mmol DPPH in methanol was added to 1 ml of different concentrations (2000, 1000, 500, 250, 125, and 62.5 μg/ml) of L1, L2, C1, C2 or reference compound. The mixture was vortexed and then incubated in a

dark chamber for 30 mins after which the absorbance was measured at 517 nm against a control containing 2 ml of methanol:

$$The\ percentage\ inhibition = \frac{Absorbance\ of\ control - Absorbance\ of sample}{Absorbance\ of\ control\ X\ 100}$$

The percentage inhibition was plotted against the Log concentration of the samples (µg/ml) to determine the $IC_{50}$, as $Log^{-1}$ x (µg/ml) from the equation: y = mx + c when y = 50.

**Antibacterial Studies**

A well-prepared McFarland 0.5 turbidity standard was compared to the inoculum with the standard visually. Mueller-Hinton Agar (MHA) was poured into the sterile petri dishes and allowed to solidify and dried for 15 minutes to remove excess moisture. The surface of the MHA plate was evenly streaked with the swab to ensure uniform growth of the bacteria using a sterile cotton swab dipped into the bacterial suspension (McFarland standard). The antimicrobial activity was carried out by an adapted agar well-diffusion method. The antimicrobial activity of the synthesized compounds was determined against (Staphylococcus aureus, Escherichia coli, Pseudomonas aeruginosa) microbial stain.

The sterile cork borer was used to punch wells (6 mm) into the inoculated MHA plate; the well was filled with varying concentrations of the Schiff base (L1, L2) and complexes (C1, C2) solutions and incubated at 37 ℃ for 18-24 hours. The activity was determined and recorded by measuring the growth in the inhibitor zone.

**Computational Studies**

The 2D guess structures of the compounds were drawn in ChemDraw and uploaded in GaussView16 interface. The optimization and frequency calculation of the clean structures were carried out using the Density Functional Theory (DFT) method and B3LYP/6-311+G (d,p) model chemistry in Gaussian09 (Frisch, et al., 2009). The online programs SwissADME (Daina et al., 2017; Daina & Zoete, 2016) and pkCSM (Pires et al., 2015) were used for the ADMET profiling of the ligands. The molecular docking studies to examine the interactions between the organic ligands against *E. coli* 6F86 (Narramore et al., 2019) and Keap1 4L7B (Jnoff et al., 2014) were carried out using the SwissDock program (Bugnon et al., 2024; Röhrig et al., 2023).

The 3D structure of the PDB: 6F86 and PDB: 4L7B were downloaded from the RCSB Protein Databank. The docking results were analyzed using ChimeraX (Meng et al., 2023; Pettersen et al., 2021) and BIOVIA Discovery Studio Analyzer software (Ercan et al., 2021).

## 3.0: Results and Discussion

### 3.1: Theoretical Insight (the Ligands)

To acquire preliminary information regarding the biological and chemical properties of the organic ligand to avoid experimental trial and error, the compounds were subjected to virtual screening such as ADMET profiling, molecular docking, and DFT calculations. The optimized structures of L1 and L2 are presented in Fig 1.

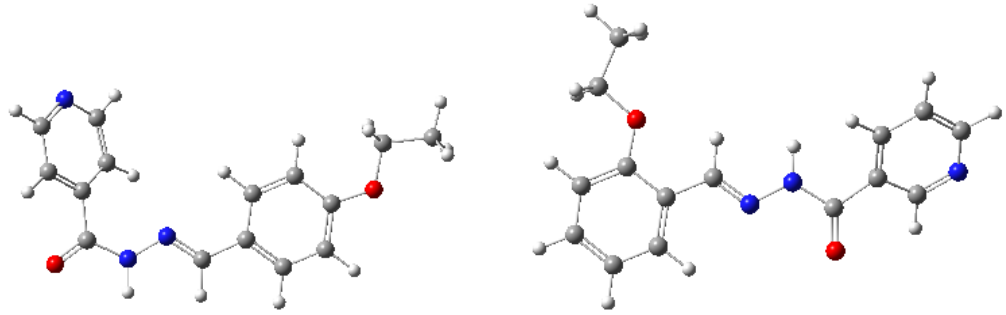

L1 L2

Figure 1: the optimized structure of L1 andL2

### 3.2: ADMET Profiling

The ADMET prediction of the compounds carried out with SwissADME and pkCSM is reported in Table 1. The results showed the compounds are promising drug candidates, they are predicted to be highly absorbed in the gastrointestinal tract, non-inhibitors of CYP3A4, readily bioavailable, non P-glycoprotein substrate, are not mutagenic and they do not interfere with hERG I and II inhibitors.

Table 1: The ADMET Properties of L1 and L2

| Property | **L1** | **L2** |
|---|---|---|
| **Physicochemical and lipophilicity** | | |
| TPSA | 63.58 | 63.58 |
| Consensus Log $P_{o/w}$ | 2.17 | 2.22 |
| ESOL Log S | -2.88 | -2.88 |
| **Pharmacokinetics** | | |
| GI Absorption | High | High |
| BBB permeant | Yes | Yes |
| P-gp substrate | No | No |
| CYP3A4 inhibitor | No | No |
| **Druglikeness** | | |
| Lipinski violations | No | No |
| Bioavailability Score | 0.55 | 0.55 |
| **Medicinal Chemistry** | | |
| PAINS alerts | 0 | 0 |
| Leadlikeness violations | 1 | 1 |
| Synthetic Accessibility | 2.34 | 2.50 |
| **Toxicity** | | |
| AMES toxicity | No | No |
| MTD (human) | 0.418 | 0.205 |
| hERG I inhibitor | No | No |
| hERG II inhibitor | No | No |
| LD50 | 2.307 | 2.634 |
| LOAEL | 1.396 | 1.415 |
| Hepatotoxicity | Yes | Yes |
| Skin Sensitisation | No | No |
| *T.Pyriformis* toxicity | 1.006 | 1.001 |
| Minnow toxicity | 1.411 | 1.936 |

The results suggest the drug candidates can be administered orally, may not cause drug-drug interaction, stay inside the cells, not damage DNA, and not block the heart's K channel. The compounds are predicted to cross the Blood-Brain Barrier and are hepatotoxic, which is common with Schiff bases (Ranjith & Ravikumar, 2019)(Mushtaq et al., 2024). Some compounds with such an initial red flag, for example, the anticancer drug venetoclax and the HIV drug Lenacapavir, scaled to clinicals and emerged as successful drugs (Bethany,

2023; David & Philip, 2021). L1 is predictably more tolerated than L2.

### 3.3: FMO, MEP, and Global reactivity parameters

The HOMO-LUMO gap obtained from FMOs calculation provides information relating to chemical reactivity and stability (Fig 2). The energy gap and lower hardness of the molecules indicate they are soft and polarizable (Table 2). L1 is softer and more polarizable than L2 because of its smaller energy gap and lower hardness (Sabry et al., 2024). This suggests that L1 will interact better with protein target especially charge transfer interactions. The electrophilicity index also predicts L1 will be stronger electrophile and should interact better with nucleophilic sites in the protein binding pocket

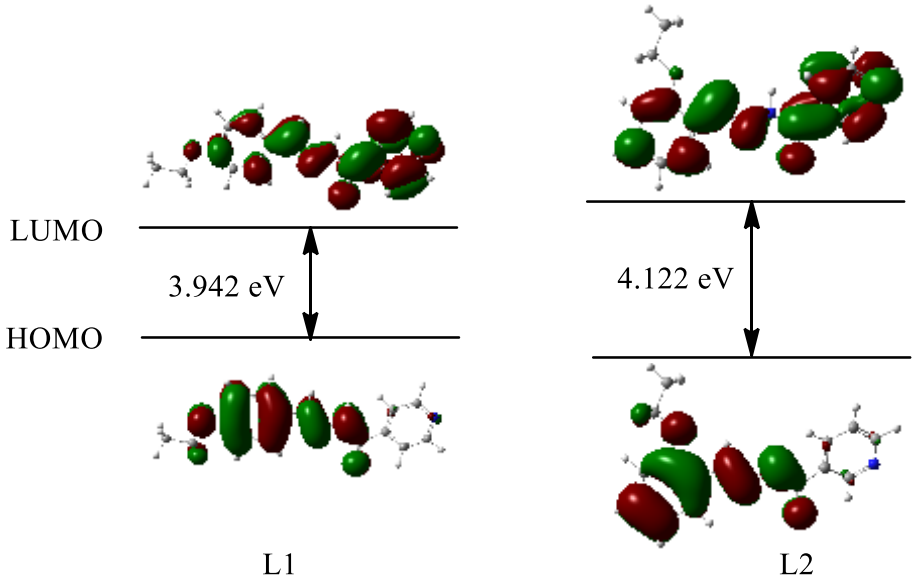


Figure 2: The FMO of L1 and L2 showing the energy gap

Table 2: Energetics and Global reactivity Parameters (in eV) calculated at the DFT/B3LYP/6-311G(d,p) model chemistry level

| Molecule | $E_{HOMO}$ | $E_{LUMO}$ | ΔE | μ | η | ω |
|---|---|---|---|---|---|---|
| L1 | -6.0624 | -2.1209 | 3.942 | -4.0917 | 1.9708 | 4.2471 |
| L2 | -6.1487 | -2.0267 | 4.122 | -4.0877 | 2.061 | 4.0537 |

The molecular electrostatic potential map of the two molecules (Fig. 3) displays distinct zones susceptible to hydrogen bonding. The carbonyl oxygen and the pyridine N are the centres of highest electron densities, with the imine proton appearing as the most electron deficient region. The higher reactivity predicted for L1 suggests it may have a potentially stronger induced interaction.

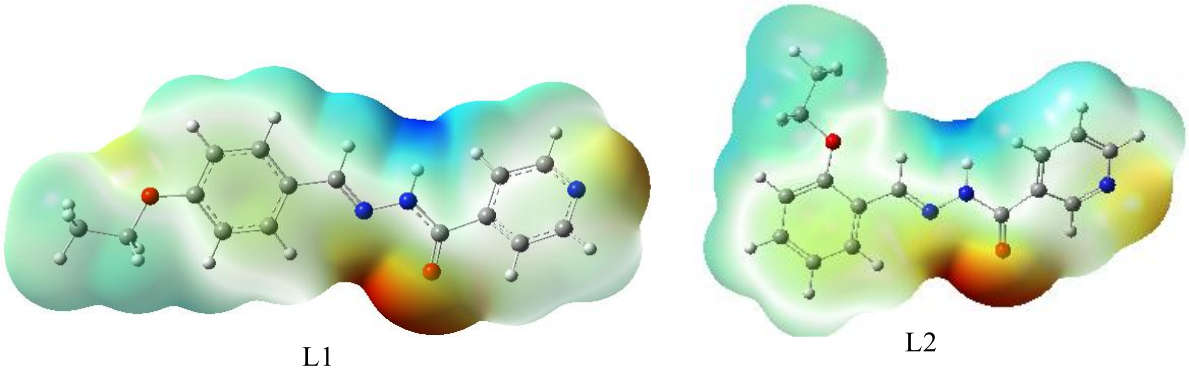


Figure 3: Molecular Electrostatic Potential Maps of the Ligands

### 3.4: Molecular Docking

The molecular docking was performed using the Activating Cavity program on SwissDock to examine the binding interactions between the studied compounds and the residues in the active sites of E. *coli* DNA gyrase B 6F86 and 4L7B (Keap1) for the antibacterial and antioxidant studies, respectively. The docking protocol was first validated by redocking the 4-(4-bromanylpyrazol-1-yl)-6-(ethylcarbamoylamino)-~{N}-pyridin-3-yl-pyridine-3-carboxamide (CWW) and (1S,2R)-2-{[(1S)-1-[(1,3-dioxo-1,3-dihydro-2H-isoindol-2-yl) methyl]-3,4-dihydroisoquinolin-2(1H)-yl] carbonyl} cyclohexanecarboxylic acid (1VV) co-crystallized ligands inhibitor in PDB: 6F86 and 4L7B respectively. The top scorer redocked ligand pose was superimposed with the protein's co-crystallized ligand of the two targets. The matching of the poses (Fig 4) is good with RMSD of 0.99Å. and 1.01 Å.

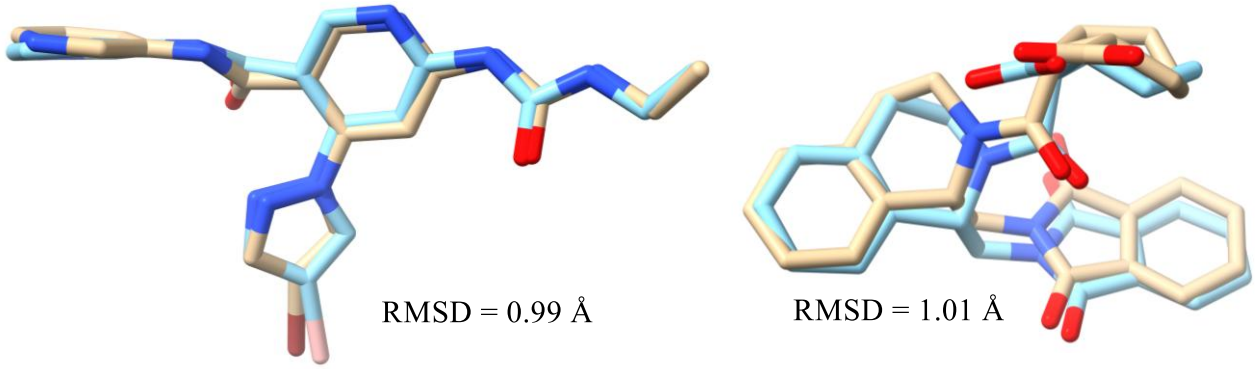


Figure 4: superimposed structures of the redocked co-crystallized CWW and 1VV in PDB: 6F86 and PDB: 4L7B, respectively, showing the RMSD.

### 3.5: Antibacterial screening

The ligands' best binding pose into the deep pocket of the PDB: 6F86 are presented in Fig 5. They both bind strongly with ASN 46. The residue is responsible for the conversion of ATP into ADP, with accompanying energy release necessary for protein survival. L1 displayed two strong hydrogen bonding

interactions with GLU50, which is a catalytic residue playing a crucial role in the protein's ATPase domain. This suggests L1 may effectively block the ATP hydrolysis process. The GLU 50 interaction in L2 points to a less effective shutting down of the reaction mechanism in the active site of the enzyme (Yuan & Hao, 2023)(Galma et al., 2021).

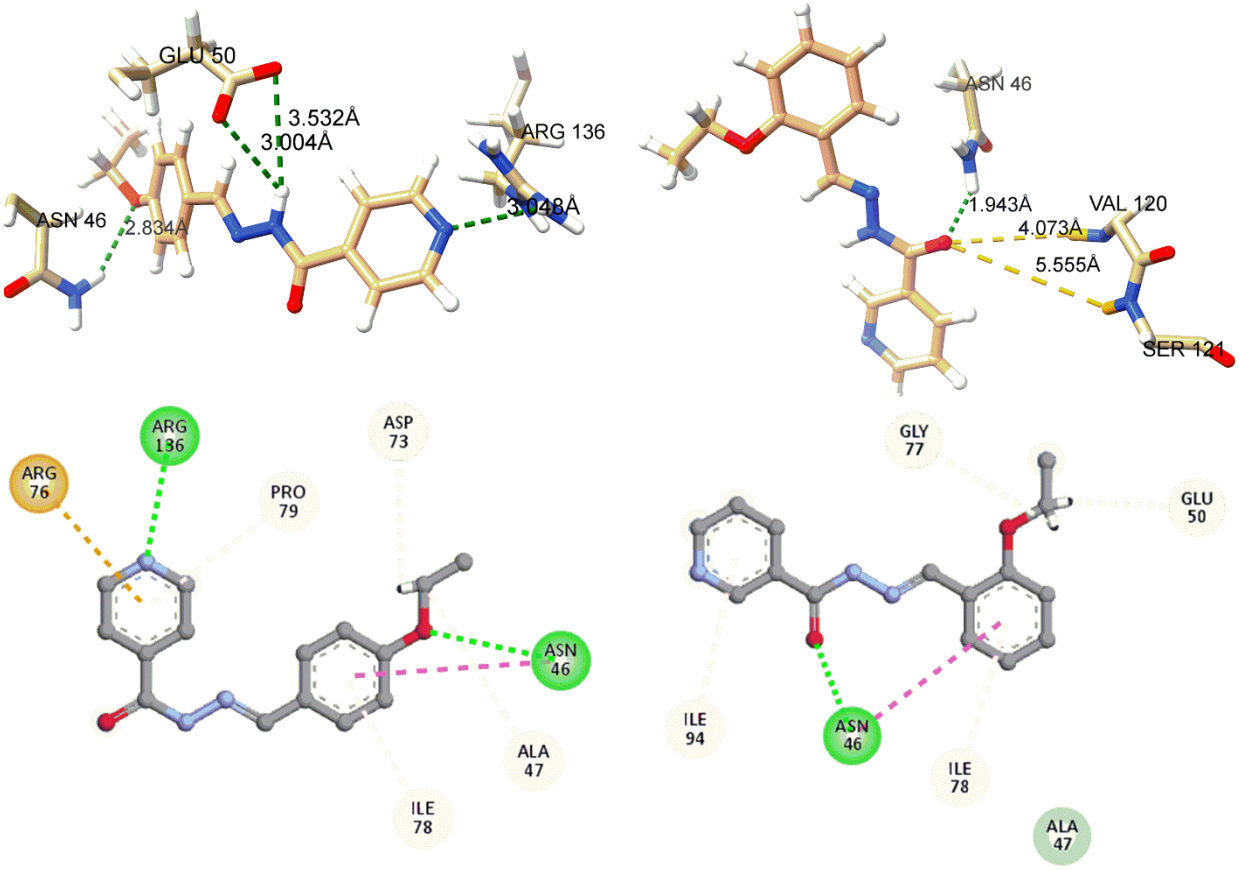


Figure 5: The 2D and 3D diagram of the binding pose of L1 and L2 with the *E. coli* DNA gyrase B 6f86

**3.6: Antioxidant Activity**

Molecular docking is well suited for studying biological pathway regulations. In our search for the mechanism of our drug candidate's action as an inhibitor to reduce oxidative stress, we selected PDB: 4L7B, a popular Kelch-like ECH-associated protein 1 (Keap1). Keap1 binds to Nrf2 and degrades it. Inhibiting Keap1 will allow Nrf2 freedom to move to the nucleus, where it activates the Antioxidant Response Element (ARE) genes, which switch on the cell's natural defence. The natural Nrf2 binder relies mainly on electrostatic interaction with Arginine residues (Arg415, Arg483, and Arg380) (Baird & Yamamoto, 2020)(Kansanen et al., 2013; Zhuang et al., 2017). The interactions of our study ligands with the active site of the target are presented in Fig 6.

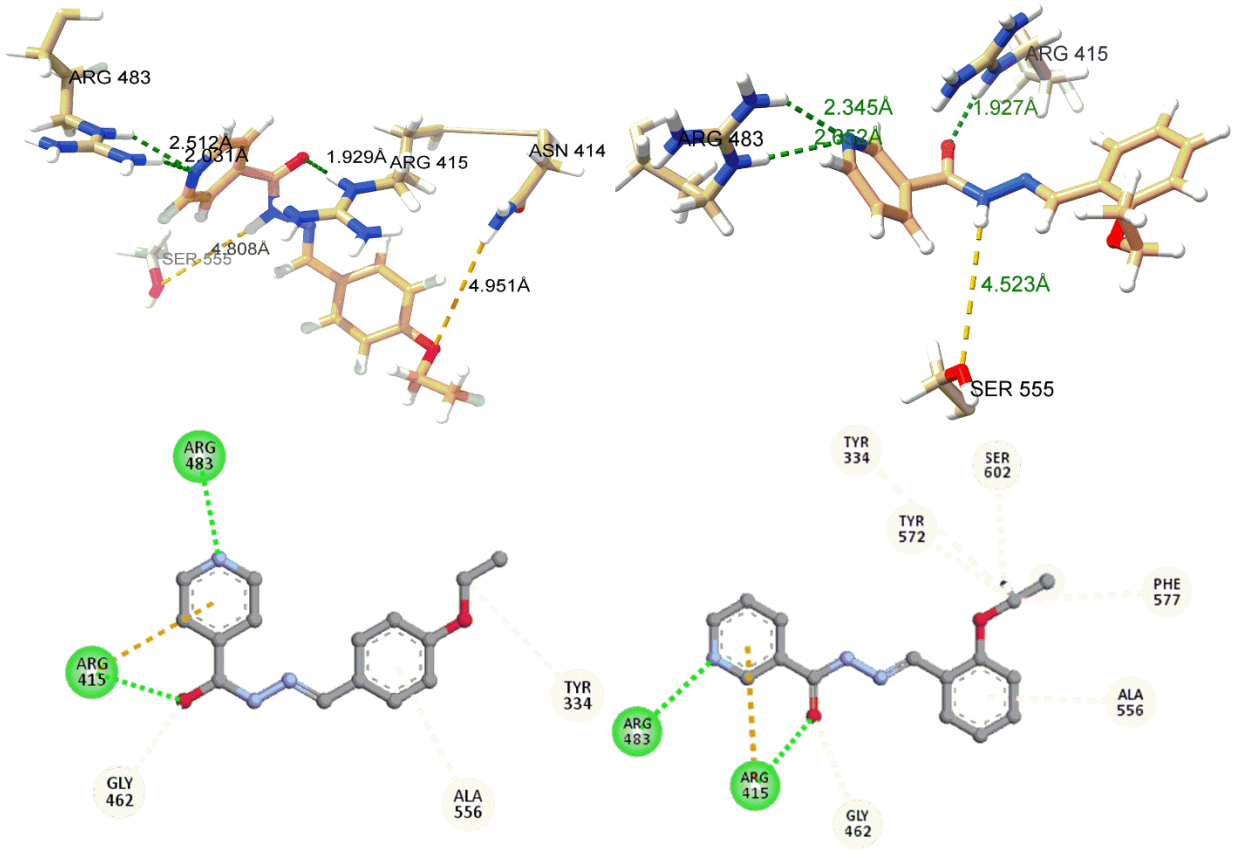


Figure 6: The 2D and 3D diagram of the binding pose of L1 and L2 with the 4L7B (Keap1)

The compounds form very strong hydrogen bonding interactions with Arg 415 (1.82, 1.92 Å) and Arg 483 (2.03, 2.34 Å). They form other weaker interactions with Tyr 334 and Ala 556. L2 forms extra interactions with Ser 602, Tyr 572, Phe 577. The strong hydrogen bonding to Arg 415 and Arg 483 signifies that the compound effectively acts like the acidic glutamate residues of the natural Nrf2 substrate(Zhuang et al., 2017). Their binding to the residues potentially blocks Nrf2, thereby releasing it for its natural antioxidant role.

### 3.7: Structure Activity Relationship

The compounds L1 and L2 differ in the positions of the N atom of the pyridine ring and the ethoxy group. In L1 the N atom is in the para position, just as the ethoxy group is in a para position to the hydrazone linker, making it somewhat linear, while L2 is bent due to the meta position of the N atom in niacin and the ortho position of the ethoxy group adjacent to the linker. The linear structure of L1 allows for easy electron flow compared to the kinked structure of L2. This accounts for the smaller HOMO-LUMO gap (3.94 eV) in L1 compared to 4.12 eV in L2.

The structure of these regioisomers affects their antibacterial and antioxidant activities. The linear shape of L1 allows it to penetrate deeper into the deep and narrow pocket of the DNA Gyrase PDB: 6F86, binding to Glu 50. The absence of this interaction in L2 is likely due to hinderances caused by the side arm

preventing the molecule from penetrating deeply to access the Glu 50 residue. For the antioxidant model, closely comparable interactions of the molecules to the shallow binding surface of PDB: 4L7B, which do not require deep penetration.

The ethoxy group may not significantly affect their activities in terms of structure. The position of the ethoxy group impacted the maximum tolerable dose. Liver enzymes often metabolize para substituted molecules better than ortho substituted analogues. Ortho derivatives can lead to the formation of reactive metabolic byproducts such as quinone methides or metal chelates in vivo. The isoniazid core is key to the biological activities; the change in the position of the N atom disrupted the electronic conjugation and the linear shape required to penetrate the binding cavity, leading to a decrease in potency.

Generally, L1 activities are likely superior to L2. In the antibacterial study, it binds more strongly to Glu 50 and An46 and to Arg 415 and Arg 483 in the antioxidant evaluations. This superiority is corroborated by its smaller HOMO-LUMO gap and higher polarizability predicted by FMOs and global reactivity parameters. These properties are reflected in its ability to act as HB Donor for the Glu 50 (acidic) in bacterial and HB acceptor from Arg 415 (basic) in human, displaying its ability to suit different protein environments due to its electronic flexibility.

However, the two compounds have shown good potential to effectively kill bacteria by inhibiting DNA Gyrase as well as protecting the patient's cells from oxidative stress and inflammation resulting from bacterial infection. The compounds are predicted to be orally bioavailable, non-mutagenic with no threat of cardiotoxicity. These promising results prompted experimental validation and development of their metal complexes to investigate the impact of improved electronic potential as a result of metal coordination on the biological activity of the two isomeric ligands.

Synthesis of the ligands

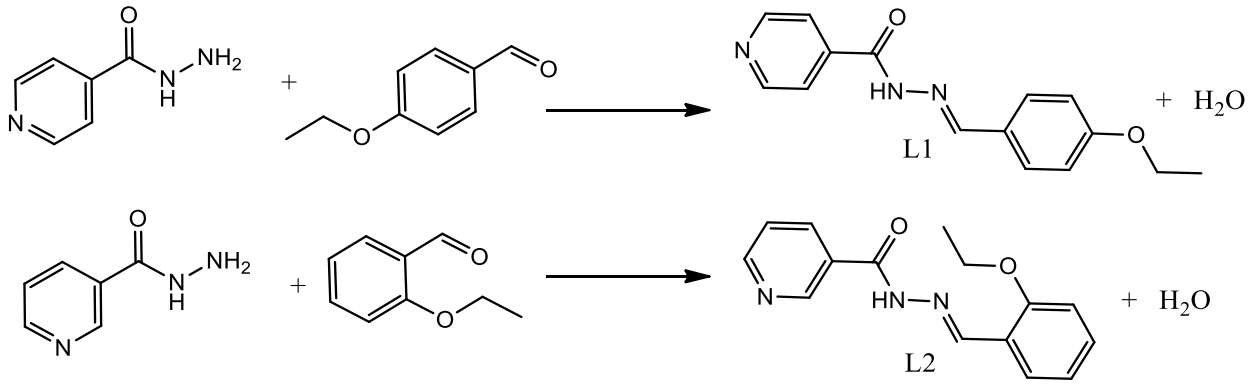


Scheme 1: Route to the synthesis of L1 and L2

The equations (1) and (2) represent the preparation of the complexes

$L1 + FeCl_3 \rightarrow Fe(L1)_n + nCl$ (1)

$L2 + LaCl3 \rightarrow La(L2)n + nCl$ (2)

**3.8: FTIR Analysis**

The spectra of the compounds displayed peaks appearing at 1645 $cm^{-1}$ and 1560 $cm^{-1,}$ and 1664 $cm^{-1}$ and 1600 $cm^{-1}$, assigned to azomethine C=N and carbonyl C=O in the spectra of L1 and L2, respectively, which is a key indication of the formation of the hydrazones (Mandewale et al., 2015; Shah et al., 2022). The unhybridized aldehyde's terminal C=O is usually found around 1700 $cm^{-1,}$ which is missing in the Spectral. The peaks at 1246 $cm^{-1}$ and 1244 $cm^{-1}$ are assigned to the ether linkage of the ethoxy group, while the weak peak at around 3200 $cm^{-1}$ is assigned to the N-H Vibration.

The difference in the carbonyl stretching vibration can be rationalized based on the computational studies' results. The lower vibrational frequency of L1 relates to the para positions of the isoniazid N atom and the ethoxy group of the benzene ring, which confers planarity on the molecule, which allows for extended conjugation across the molecule. This results in a lower frequency. In L2, the position of these constituents distorts the structure, breaking the conjugation and leading to a higher frequency.

**3.9: NMR Analysis**

The $^1H$ NMR spectra corroborated the FTIR result in confirming the formation of the Schiff base, with the diagnostic amide and azomethine peaks displayed downfield > 8 ppm. The sharp singlet (δ 8.45 s 1H) in L1 represents the azomethine proton, which was slightly deshielded further to (δ 8,65, s 1H) in L2, likely due to the proximity of the O atom of the ethoxy group (Munir et al., 2021). The downfield singlets (δ ll.98, s 1H) and (δ ll.96, s 1H) correspond to the amide proton of L1 and L2 hydrazide, respectively.

The environment of the four protons on the pyridine ring is important in the 1H NMR characterization of these compounds. The signal at (δ 8.78 d, 2H) is assigned to the 2 protons adjacent to the pyridine N, while the other doublet (δ 7.82 d, 2H) is assigned to the next proton neighbour at positions 3 and 5 in L1. In L2, the four protons on the pyridine ring are in distinct chemical environments. The singlet (δ 9.08 s H) is assigned to the proton saddled between the nicotine rings N and the carbonyl group. This significantly distinguished L2 from L1, confirming the position of the N in the two rings. The three other protons appeared at 8.75, 8.25, and a multiplet at 7.55 ppm.

The Signals at (δ 7.65 d 2H) and (δ 7.04 d 2H) in L1 spectra are assigned to the 2 H on the phenyl ring closest to the imine linkage and the other two next to the ethoxy group, respectively (Luppi et al., 2007). The latter set is thought to be shifted upfield by the electron-donating oxygen atom of the ethoxy group. In L2, because the ethoxy group is not substituted at the para position like L1 the four phenyl protons are non-equivalents. They appear in overlapping modes between 6.9-7.9 ppm. The ethoxy protons appeared as (δ 4.12 q, 2H) and (δ 1.35 t, 3H), respectively, indicating

the distinct environment of the methylene and methyl protons, respectively, in both compounds.

In the complexes' spectra, the sharp singlet at δ11.98 in C1 corresponding to the amide proton L1 is extremely weak and broadened in C1 spectrum, signifying L2 undergoes conversion from the keto form to the enol form and subsequent deprotonation to coordinate Fe. In C2, this peak resonates at around D12 ppm with an integral of 1. This is an indication that the proton is retained in the complex, that is, the L2 coordinates to the metal La in the neutral keto form. Additionally, the azomethine proton, which appeared at 8.65 ppm in the free ligand, shifted downfield to 8.8 ppm in the complex C2 spectrum. This is thought to be due to the reduction of electron density around the proton as a result of electron pair donation by N to the La centre.

The $^{13}C$ spectrum of C1 also displayed broadened signals. The shift in carbonyl and azomethine carbon are further proof of coordination. The exact shifts are not easy to ascertain due to the paramagnetic influence of the $Fe^{3+}$. This is not so with C2, with $La^{3+}$, a $4f^0$ diamagnetic specie, where the distinct positions from those of the L2 are clear. The peaks corresponding to C=O (160-165 ppm) and C=N (145-150) represent shifts upon coordination.

### 3.10: Antibacterial Activity

The experimental antibacterial activity of the ligands and the metal complexes against E coli strain is displayed on Table x and visually displayed in the bar chart (Fig 7). The result revealed significant activities and a trend consistent with the molecular docking results. L1 exhibited the highest antibacterial efficacy, followed by its complex C1 and L2. Curiously, the E coli strain showed resistance to the complex C2 at all concentrations, and C1 showed less efficacy compared to the ligand L1. This is contrary to expectations, as the metal complexes are supposed to be more lipophilic, making easy access to the target cavity. The inability of the bulky iron complex to fit into the slim binding pocket of DNA Gyrase may be responsible for the reduced activity of C1. The bulkier C2 will therefore find it impossible to penetrate the narrow pocket of the 6F86 due to steric hindrance despite its lipophilicity.

Table 3: the bactericidal activity of the ligands and complexes against E. coli

| **Concentration (μM)** | **Percentage Inhibition** | | | |
|---|---|---|---|---|
| | **L1** | **L2** | **C1** | **C2** |
| 2000 | 30 | 20 | 24 | R |
| 1000 | 24 | 12 | 10 | R |
| 500 | 15 | 10 | 10 | R |
| 250 | 10 | 6 | 6 | R |
| CONTROL μM | 24.5 | 23 | 21 | 21 |

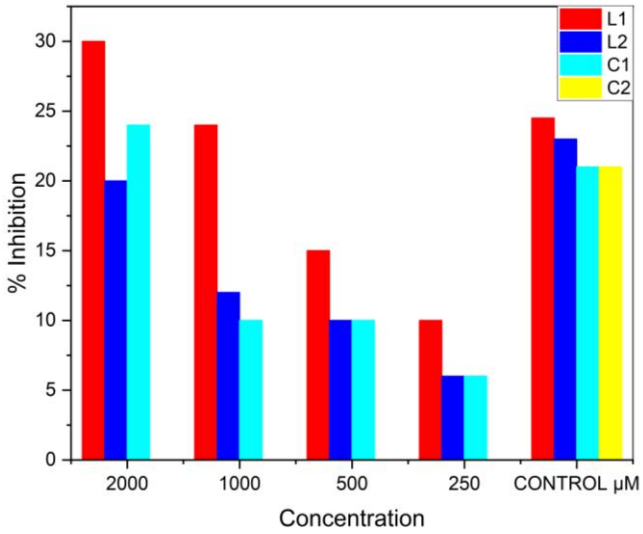


Figure 7: The antibacterial action of the metal and complexes

**3.11: Antioxidant Activity**

The metal complexes displayed significantly better antioxidant activity compared to the free organic molecules. The trend of activity according to the results displayed in Table 4 and Fig 8 is C1>C2>L1>L2. The ligands' trend is also consistent with the molecular docking result against Keap1 4L7B, where L1 outperformed L2. The increased activities on complexation can be ascribed to redox cycling of C1 and stabilization of radical-ligand intermediate in the redox-inert C2. The performance of the metal species confirms that coordination compounds have better antioxidant character than pure organic molecules.

Table 4: Antioxidant Activity of the ligands and complexes

| | Conc µg/ml | Percentage Inhibition | | | |
|---|---|---|---|---|---|
| | | L1 | L2 | C1 | C2 |
| 1 | 2000 | 11.88 | 9.00 | 15.18 | 12.01 |
| 2 | 1000 | 5.44 | 5.01 | 13.48 | 12.90 |
| 3 | 500 | 3.45 | 4.74 | 8.70 | 9.21 |
| 4 | 250 | 2.68 | 4.39 | 3.30 | 3.97 |
| 5 | 125 | 1.83 | 3.81 | 2.45 | 3.25 |
| 6 | 62.5 | 1.71 | 3.26 | 1.59 | 2.23 |

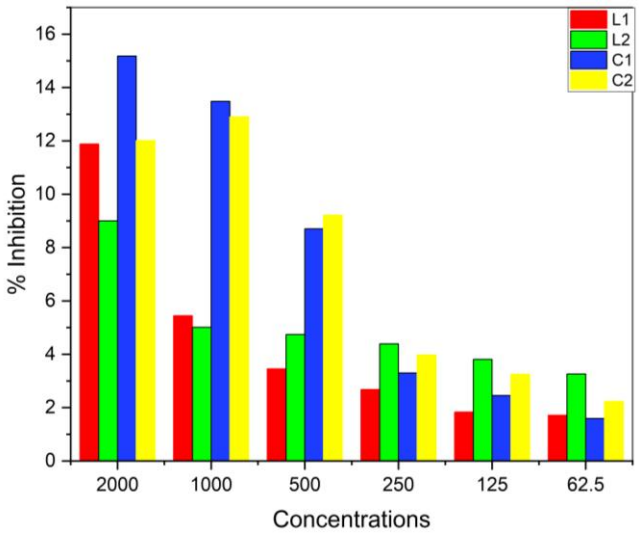


Figure 8: The antioxidant action of the metals and complexes

**4.0: Conclusion**

This study successfully used a theoretical and experimental approach to demonstrate the role of positional isomerism and metal chelation on the pharmacological efficacy of two pyridine-based hydrazones and their metal complexes. Experimental FTIR and NMR analysis revealed that the carbonyl stretching frequency (1645 $cm^{-1}$) of L1, the isoniazid derivatized specie confirmed a planar and highly conjugated and somewhat linear geometry, while the carbonyl frequency for the nicotinic analogue appearing at a higher frequency (1664 $cm^{-1}$) revealed a bent structure caused by the position of the ethoxy group and N atom in the pyridine ring. The $^{1}H$ NMR analysis revealed distinct coordination modes; the Fe(III) coordinated the enol form of L1 in a paramagnetic environment, while the La(III) adopted the keto form in a diamagnetic environment.

The experimental antibacterial and antioxidant evaluations revealed highly corroborated results with the computational predictions. Experimental antibacterial assays confirmed that the linear isoniazid isomer is significantly more potent than the bent nicotinic hydrazide isomer against E. coli. Notably, L1 exhibited superior performance compared to the standard drug at high concentrations validating th molecular docking results that its linear shape facilitated a deep penetration into the DNA Gyrase B binding pocket.

The antioxidant experiment revealed that while the free organic ligands displayed moderate activity, complexation with metal significantly improved their scavenging potential. The most potent antioxidant performance by C1 is likely due to the redox-active nature of the Fe centre.

The foregoing establishes the 4-ethoxybenzylidene isonicotinohydrazide as a promising lead scaffold. Its para N and ethoxy group confer the linear position required for potent antibacterial action, while its metal complex is a powerful antioxidant. These findings are confirmation that regioisomerism is a decisive factor in the design of dual action therapeutics for multidrug resistant infections and oxidative stress.

**5.0: Acknowledgement**

Gabriel K. Obiyenwa and T. A. Abubakar express profound appreciation to the Tertiary Education Trust Fund (Tetfund) Nigeria, for the Institutional Based Research (IBR) grant.

**6.0: References**

Arogba, S. S., & Omede, A. (2012). Comparative Antioxidant Activity of Processed Mango (Mangifera indica) and Bush Mango (Irvingia gabonensis) Kernels. *Nigerian Food Journal*, *30*(2), 17–21. https://doi.org/10.1016/s0189-7241(15)30029-1

Baird, L., & Yamamoto, M. (2020). The Molecular Mechanisms Regulating the KEAP1-NRF2 Pathway. *Molecular and Cellular Biology*, *40*(13), 1–23. https://doi.org/https://doi.org/10.1128/MCB.00099-20

Bethany, H. (2023). Wrestling with Lipinski ' s rule of 5. *C&en*, *101*(8). https://doi.org/10.1016/S0169-409X(96)00423-1

Bugnon, M., Röhrig, U. F., Goullieux, M., Perez, M. A. S., Daina, A., Michielin, O., & Zoete, V. (2024). SwissDock 2024: major enhancements for small-molecule docking with Attracting Cavities and AutoDock Vina. *Nucleic Acids Research*, *52*(W1), W324–W332. https://doi.org/10.1093/nar/gkae300

Daina, A., Michielin, O., & Zoete, V. (2017). SwissADME : a free web tool to evaluate pharmacokinetics , drug- likeness and medicinal chemistry friendliness of small molecules. *Nature Publishing Group*, *7*(January), 42717. https://doi.org/10.1038/srep42717

Daina, A., & Zoete, V. (2016). A BOILED-Egg To Predict Gastrointestinal Absorption and Brain Penetration of Small Molecules. *ChemMedChem*, *11*, 1117–1121. https://doi.org/10.1002/cmdc.201600182

David, A. D., & Philip, B. C. (2021). *Drug Discovery Beyond The Rule Of Five*. https://doi.org/10.1002/0471266949.bmc258

Fan, G., & Yan, D. (2014). Positional isomers of cyanostilbene: two-component molecular assembly and multiple-stimuli responsive luminescence. *Scientific Africa*, *4*, 4933. https://doi.org/10.1038/srep04933

Frei, A., Zuegg, J., Elliott, A. G., Baker, M., Braese, S., Brown, C., Chen, F., Dowson, C. G., Dujardin, G., Jung, N., King, A. P., Mansour, A. M., Massi, M., Moat, J., Mohamed, H. A., Renfrew, A. K., Rutledge, P. J., Sadler, P. J., Todd, M. H., … Blaskovich, M. A. T. (2020). Metal complexes as a promising source for new antibiotics. *Chemical Science*, *11*, 2627–2639. https://doi.org/10.1039/C9SC06460E

Galma, W., Endale, M., Getaneh, E., Eswaramoorthy, R., & Assefa, T. (2021). Antibacterial and antioxidant activities of extracts and isolated compounds from the roots extract of Cucumis prophetarum and in silico study on DNA gyrase and human. *BMC Chemistry*, *15*(32), 1–17. https://doi.org/10.1186/s13065-021-00758-x

Kansanen, E., Kuosmanen, S. M., Leinonen, H., & Levonen, A. (2013). Redox Biology The Keap1-Nrf2 pathway : Mechanisms of activation and dysregulation in cancer $. *Redox Biology*, *1*(1), 45–49. https://doi.org/10.1016/j.redox.2012.10.001

Luppi, L. I., Hardmeier, I., Babay, P. A., & Erijman, L. (2007). Anaerobic nonylphenol ethoxylate degradation coupled to nitrate reduction in a modified biodegradability batch test. *Chemosphere*, *68*, 2136–2143. https://doi.org/10.1016/j.chemosphere.2007.01.078

M. J. Frisch, G. W. Trucks, H. B. Schlegel, G. E. S., M. A. Robb, J. R. Cheeseman, G. Scalmani, V. Barone, B. M., G. A. Petersson, H. Nakatsuji, M. Caricato, X. Li, H. P. H., A. F. Izmaylov, J. Bloino, G. Zheng, J. L. Sonnenberg, M. H., M. Ehara, K. Toyota, R. Fukuda, J. Hasegawa, M. Ishida, T. N., Y. Honda, O. Kitao, H. Nakai, T. Vreven, J. A. Montgomery, J., J. E. Peralta, F. Ogliaro, M. Bearpark, J. J. Heyd, E. B., K. N. Kudin, V. N. Staroverov, T. Keith, R. Kobayashi, J. N., K. Raghavachari, A. Rendell, J. C. Burant, S. S. Iyengar, J. T., M. Cossi, N. Rega, J. M. Millam, M. Klene, J. E. Knox, J. B. C., V. Bakken, C. Adamo, J. Jaramillo, R. Gomperts, R. E. S., O. Yazyev, A. J. Austin, R. Cammi, C. Pomelli, J. W. O., R. L. Martin, K. Morokuma, V. G. Zakrzewski, G. A. V., P. Salvador, J. J. Dannenberg, S. Dapprich, A. D. D., O. Farkas, J. B. Foresman, J. V. Ortiz, J. C., & Fox, and D. J. (2021). *Gaussian 09, Revision D.01,*. *6*(3), 132–136.

Mandewale, M. C., Thorat, B., Shelke, D., & Yamgar, R. (2015). Synthesis and Biological Evaluation of New Hydrazone Derivatives of Quinoline and Their Cu ( II ) and Zn ( II ) Complexes against Mycobacterium tuberculosis. *Bioinorganic Chemistry and Applications*, *2015*. https://doi.org/10.1155/2015/153015

Meng, E. C., Goddard, T. D., Pettersen, E. F., Couch, G. S., Pearson, Z. J., Morris, J. H., & Ferrin, T. E. (2023). UCSF ChimeraX: Tools for structure building and analysis. *Protein Science*, *32*(11), 1–13. https://doi.org/10.1002/pro.4792

Munir, R., Javid, N., Zia-ur-rehman, M., Zaheer, M., Huma, R., Roohi, A., & Athar, M. M. (2021). Synthesis of Novel N - Acylhydrazones and Their C-N/N-N Bond Conformational Characterization by NMR Spectroscopy. *Molecules*, *26*(4908). https://doi.org/https://doi.org/10.3390/molecules26164908

Mushtaq, I., Ahmad, M., Saleem, M., & Ahmed, A. (2024). Pharmaceutical significance of Schiff bases : an overview. *Future Journal of Pharmaceutical Sciences*, *10*(16). https://doi.org/10.1186/s43094-024-00594-5

Narramore, S., Stevenson, C. E. M., Maxwell, A., Lawson, D. M., & Fishwick, C. W. G. (2019). New insights into the binding mode of pyridine-3-carboxamide inhibitors of E. coli DNA gyrase. *Bioorganic and Medicinal Chemistry*, *27*(16), 3546–3550. https://doi.org/10.1016/j.bmc.2019.06.015

Nidhi, S., Pratap, D., Kumar, A., & Verma, A. (2025). Results in Chemistry Schiff bases and their possible therapeutic applications : A review. *Results in Chemistry*, *13*(September 2024), 101941. https://doi.org/10.1016/j.rechem.2024.101941

Pettersen, E. F., Goddard, T. D., Huang, C. C., Meng, E. C., Couch, G. S., Croll, T. I., Morris, J. H., & Ferrin, T. E. (2021). UCSF ChimeraX: Structure visualization for researchers, educators, and developers. *Protein Science*, *30*(1), 70–

82. https://doi.org/10.1002/pro.3943

Pires, D. E. V, Blundell, T. L., & Ascher, D. B. (2015). pkCSM: Predicting Small-Molecule Pharmacokinetic and Toxicity Properties Using Graph-Based Signatures. *Journal of Medicinal Chemistry*, *58*, 4066–4072. https://doi.org/10.1021/acs.jmedchem.5b00104

Ranjith, C., & Ravikumar, D. (2019). SwissADME predictions of pharmacokinetics and drug-likeness properties of small molecules present in Ipomoea mauritiana Jacq. *Journal of Pharmacognosy and Phytochemistry*, *8*(5), 2063–2073.

Reema, S., Sing Sara, U. V., L., K. R., James, S., & Jain, J. (2011). Nicotinic Acid Hydrazones: A Novel Anticonvulsant Pharmacophore. *Med Chem Res*, *20*, 1499–1504. https://doi.org/10.1007/s00044-010-9396-0

Röhrig, U. F., Goullieux, M., Bugnon, M., & Zoete, V. (2023). Attracting Cavities 2.0: Improving the Flexibility and Robustness for Small-Molecule Docking. *Journal of Chemical Information and Modeling*, *63*(12), 3925–3940. https://doi.org/10.1021/acs.jcim.3c00054

Sabry, N. M., Badry, R., Abdel-gawad, F. K., Elhaes, H., & Ibrahim, M. A. (2024). Electronic structure , global reactivity descriptors and nonlinear optical properties of glycine interacted with ZnO , MgO and CaO for bacterial detection. *Scientific Reports*, *14*(22801), 1–24.

Shah, M. A., Ala, U., Muhammad, R. S., Imdad, A., Riaz, U., Hannan, P. A., & Hussain, H. (2022). Synthesis and Characterization of Novel Hydrazone Derivatives of Isonicotinic Hydrazide and Their Evaluation for Antibacterial and Cytotoxic Potential. *Molecules*, *27*, 6770. https://doi.org/https://doi.org/10.3390/ molecules27196770

Waziri, I., Nthehang, T. S., Oyedeji-amusa, M. O., Oyebamiji, A. K., Adeyinka, A. S., & Muller, A. A. (2025). Computational Study of Mo ( VI ) Complexes Derived from Hydrazone Schiff Base Ligands. *ChemistrySelect*, *10*(e01578), 1–20. https://doi.org/10.1002/slct.202501578

Yuan, C., & Hao, X. (2023). Heliyon Antibacterial mechanism of action and in silico molecular docking studies of Cupressus funebris essential oil against drug resistant bacterial strains. *Heliyon*, *9*(8), e18742. https://doi.org/10.1016/j.heliyon.2023.e18742

Zhuang, C., Wu, Z., Xing, C., & Miao, Z. (2017). Small molecules inhibiting Keap1–Nrf2 protein–protein interactions: a novel approach to activate Nrf2 function. *MedChemComm*, *8*, 286–294. https://doi.org/10.1039/C6MD00500D